



# Mesoporous manganese oxides prepared by solution combustion synthesis as catalysts for the total oxidation of VOCs



Marco Piumetti, Debora Fino, Nunzio Russo\*

Department of Applied Science and Technology, Politecnico di Torino, Corso Duca degli Abruzzi 24, 10129 Torino, Italy

## ARTICLE INFO

### Article history:

Received 9 June 2014

Received in revised form 31 July 2014

Accepted 7 August 2014

Available online 15 August 2014

### Keywords:

Manganese oxides

Catalytic oxidation of VOCs

Monolithic catalyst

Solution combustion synthesis

Redox mechanism

## ABSTRACT

Three mesoporous manganese oxide catalysts ( $\text{Mn}_2\text{O}_3$ ,  $\text{Mn}_3\text{O}_4$  and  $\text{Mn}_x\text{O}_y$ ) have been prepared, by means of the solution combustion synthesis, and tested for the total oxidation of volatile organic compounds (VOCs; ethylene, propylene, toluene and their mixture). The best results, in terms of the total oxidation of VOCs, were achieved with the  $\text{Mn}_3\text{O}_4$  catalyst, which showed the highest amount of electrophilic oxygen on the surface ( $\text{O}_\alpha$ -species).

The most active powder catalyst was then deposited on a cordierite-type monolith through a novel direct synthesis and tested for the total oxidation of the VOCs mixture. The  $\text{Mn}_3\text{O}_4$ -based monolith exhibited high activity towards the total oxidation of VOCs, which is comparable to that obtained with powdered  $\text{Mn}_3\text{O}_4$ . The monolithic catalyst showed excellent catalytic activity for the total combustion of the mixture of VOCs (conversion to  $\text{CO}_2 = 99.2\% \pm 0.5$ ) over a time-on-stream of 10 h at  $310^\circ\text{C}$  and no deactivation occurred during this time span.

© 2014 Elsevier B.V. All rights reserved.

## 1. Introduction

Volatile organic compounds (VOCs) are a large group of low molecular-weight organic chemicals that are emitted from a great variety of sources, such as industrial processes, transport, household activities and so on [1]. Nowadays, over 300 chemicals are listed as VOCs by the U.S. Environmental Protection Agency and most of them are considered as major contributors to air pollution [2–4]. Many VOCs are toxic and some are considered to be carcinogenic, mutagenic or teratogenic [4,5]. VOC emissions can contribute to photochemical smog, stratospheric ozone depletion and to the formation of tropospheric ozone [6,7]. For these reasons, VOCs are carefully regulated and several abatement technologies (i.e. adsorption, thermal oxidation, wet scrubbing, photocatalysis, catalytic oxidation, plasma oxidation, etc.) are used to control their release into the atmosphere [2,3].

Catalytic oxidation is considered one of the most effective techniques for VOC removal, since the total oxidation of diluted fuel occurs at relatively low temperatures, and this leads to low emissions of  $\text{NO}_x$  and unburned fuels [8–11]. This abatement technique is highly versatile, and offers the possibility of treating waste streams with different VOC concentrations and effluent flow rates

[2–4]. Many materials have therefore been investigated for VOC oxidation, and several catalysts, based on supported noble metals (mainly Pt and Pd) and transition metal oxides (i.e. V, Ce, Mn, Cr, Cu, Co, Ni and W), have been developed [2]. The former, though very active and selective, are too expensive and undergo deactivation by chlorinated compounds in the gas stream [12]; the latter are more resistant to deactivation by poisoning (i.e. chlorine) but are often less active [13].

Literature reports that manganese oxides may offer promising catalytic activity towards the total oxidation of VOCs [14–22]. Manganese oxide catalysts, such as  $\text{Mn}_3\text{O}_4$  [23],  $\text{Mn}_2\text{O}_3$  [24] and  $\text{MnO}_2$  [25], are known to exhibit high performances in the catalytic combustion of VOCs [26]. S.H. Kim et al. [21] have reported that the reactivity of manganese oxides shows an order of  $\text{Mn}_3\text{O}_4 > \text{Mn}_2\text{O}_3 > \text{MnO}_2$  in the total oxidation of benzene and toluene. Similarly, Ramesh et al. [27] have observed that the reactivity shows an order of  $\text{Mn}_2\text{O}_3 > \text{MnO}_2 > \text{MnO}$  in CO oxidation.

According to the literature, the most active manganese oxide catalysts are those that present the best redox properties and the highest oxygen mobility [14–26]. In fact, VOC oxidation over these catalysts usually occurs through a Mars and van Krevelen (MVK) mechanism [28], where the hydrocarbon molecule is oxidized by lattice oxygen from the manganese oxide. The lattice oxygen is then replenished by the reduction of gaseous oxygen [16,29–31]. Therefore, the availability and reactivity of surface oxygen species affect the activity of manganese oxides to a great extent [32–34].

\* Corresponding author. Tel.: +39 011 0904710; fax: +39 011 0904699.  
E-mail address: [nunzio.russo@polito.it](mailto:nunzio.russo@polito.it) (N. Russo).

**Table 1**  
Synthesis conditions used for the preparation of the catalysts.

Catalyst	Mn(NO <sub>3</sub> ) <sub>2</sub> (g)	C <sub>2</sub> H <sub>5</sub> NO <sub>2</sub> (g)	Oven temperature (°C)	Oven timer (min)
Mn <sub>2</sub> O <sub>3</sub>	2.50	0.38	600	20
Mn <sub>3</sub> O <sub>4</sub>	2.50	1.50	500	30
Mn <sub>x</sub> O <sub>y</sub>	2.50	1.50	350	120

In the present work, a set of manganese oxide catalysts has been prepared, by the so-called “Solution Combustion Synthesis” (SCS) method, and tested for the total oxidation of ethylene, propylene and toluene. These compounds were chosen as probe molecules for the catalytic activity tests because they are often found in industrial exhausts and have a high POCP (photochemical ozone creation potential) [1,35,36]. The structural and surface properties of the prepared catalysts were then investigated by means of complementary physico-chemical techniques. The most active powder catalyst was then deposited on a cordierite type monolith through a new direct synthesis (SCS route) and tested in a laboratory-scale pilot plant reactor, using the catalytic combustion of the VOC mixture (ethylene, propylene and toluene) as a test reaction.

## 2. Experimental

### 2.1. Catalysts preparation

Three manganese oxide catalysts (hereafter referred to as Mn<sub>2</sub>O<sub>3</sub>, Mn<sub>3</sub>O<sub>4</sub> and Mn<sub>x</sub>O<sub>y</sub>, in which the latter contains both Mn<sub>2</sub>O<sub>3</sub> and MnO<sub>2</sub> phases) were synthesized by means of solution combustion synthesis (SCS) [37] considering different synthesis conditions, as summarized in Table 1. In a typical synthesis, suitable amounts of Mn(NO<sub>3</sub>)<sub>2</sub> (Sigma-Aldrich) and C<sub>2</sub>H<sub>5</sub>NO<sub>2</sub> (Sigma Aldrich) were dissolved in 50 mL of deionized water and stirred at room temperature for 30 min. The homogeneous solution was then placed in an oven. The reaction was carried out at a constant temperature for a certain period time. The resultant powder was washed with distilled water to remove impurities and then dried overnight.

The powder catalyst that showed the best catalytic activity towards total VOC oxidation (Mn<sub>3</sub>O<sub>4</sub>) was deposited on a lab-scale monolith via direct SCS. A cylindrical cordierite honeycomb with the following dimensions was used: 2.5 cm length, 3.4 cm diameter and 200 cpsi cell density. In a typical synthesis 2.5 g Mn(NO<sub>3</sub>)<sub>2</sub> (Sigma-Aldrich) and 1.5 g C<sub>2</sub>H<sub>5</sub>NO<sub>2</sub> (Sigma-Aldrich) were dissolved in 50 mL of deionized water and stirred at room temperature for 30 min. The monolith was then dipped into the slurry solution so that the precursors could enter the inner channels. The monolith was then placed in an oven and left at 500 °C for 30 min. Finally, the monolith was cooled at r.t. and any excess powder was removed using compressed air. This procedure was repeated twice in order to obtain a higher amount of the active phase (final amount of Mn<sub>3</sub>O<sub>4</sub> loaded onto the monolith = 0.48 g)

### 2.2. Catalyst characterization

The X-ray diffraction patterns of the powders were collected on an X'Pert Philips PW3040 diffractometer using Cu K<sub>α</sub> radiation (2θ range = 20–70°; step = 0.05° 2θ; time per step = 0.2 s). The XRD patterns were indexed according to the Powder Data File database (PDF 2000, International Centre of Diffraction Data, Pennsylvania). The average size of the crystallites was determined using the Scherrer formula,  $D = 0.9(\lambda/b\cos\theta)$ , where  $\lambda$  is the wavelength of the Cu K<sub>α</sub> radiation,  $b$  is the full width at half maximum (in radians), 0.9 is the shape factor for spherical particles and  $\theta$  is the angle of the diffraction peaks.

The specific surface area ( $S_{\text{BET}}$ ), total pore volume ( $V_p$ ) and average pore diameter ( $D_p$ ) were measured by N<sub>2</sub> physisorption at –196 °C (Micrometrics ASAP 2020) on powders previously outgassed at 200 °C for 4 h to remove water and other atmospheric contaminants.  $S_{\text{BET}}$  was determined according to the Brunauer–Emmett–Teller (BET) method;  $V_p$  was calculated at  $p/p_0 = 0.97$ , whereas the micropore volume ( $V_{\text{micro}}$ ) was measured according to  $t$ -plot method.  $D_p$  was attained by the Density Functional Theory (DFT) method.

Samples morphology was investigated by a field emission scanning electron microscope (FESEM Zeiss MERLIN, Gemini-II column) and a Transmission Electron Microscopy (TEM, Jeol JEM 3010 operating at 200 kV).

Temperature-programmed analyses were carried out in a Thermoquest TPD/R/O 1100 analyzer, equipped with a thermal conductivity (TCD) detector. In order to perform the H<sub>2</sub>-TPR experiments, a 50 mg sample was placed in a quartz tube, put in contact with reducing flowing gas (4.95% molar H<sub>2</sub> in Ar, 40 cm<sup>3</sup> min<sup>–1</sup>) and then heated in the 20–950 °C temperature range (heating rate: 5 °C min<sup>–1</sup>), while recording H<sub>2</sub> consumption using a thermal conductivity detector (TCD). In order to perform temperature programmed oxygen desorption (O<sub>2</sub>-TPD) measurements, a 50 mg catalyst was treated under an O<sub>2</sub> flow (40 cm<sup>3</sup> min<sup>–1</sup>) at the calcination temperature for 30 min and subsequently cooled to 25 °C under the same oxygen flow rate. TPD analysis was carried out by heating the sample to 950 °C at a constant rate of 5 °C min<sup>–1</sup> under He flow.

XPS (X-ray photoelectron spectroscopy) measurements were performed on an XPS PHI 5000 Versa probe apparatus using a band-pass energy of 187.85 eV, a 45° take off angle and a 100.0 μm diameter X-ray spot size. Curve-fits were performed by means of Multipack 9.0 software.

IR spectra were collected on an FT-IR spectrophotometer (Equinox 55, Bruker), equipped with an MCT (Mercury Cadmium Telluride) cryodetector. In order to perform IR measurements, powder samples were pressed into thin self-supporting wafers (density of about 10 mg cm<sup>–2</sup>) and outgassed at 150 °C in a standard vacuum frame (residual pressure below 10<sup>–3</sup> mbar) using IR cells equipped with KBr windows. The outgassing temperature was chosen in order to preserve the Brønsted acidic sites, which are removed at higher temperatures. NH<sub>3</sub> adsorption was run at room temperature on samples outgassed at 150 °C by dosing increasing amounts of ammonia (partial pressure in the 0.00–30.0 mbar range) and by evacuating the reversible fraction of the adsorbate.

### 2.3. Catalytic activity tests

Catalytic tests were performed in a continuous reactor, that is, a quartz U-tube with an inner diameter = 4 mm, heated by an electric furnace; the temperature was measured by a thermocouple placed close to the middle of the catalytic bed. The catalyst (0.2 g, 250–450 μm particle size) was pre-treated in helium (flow rate = 100 cm<sup>3</sup> min<sup>–1</sup>) for 1 h at 100 °C to remove any species adsorbed on the catalyst surface. The gas flow was then switched from helium to the reactive mixture: 1000 ppm VOCs (ethylene, propylene and toluene or their mixture) diluted in air was fed to the reactor with a gas hourly space velocity (GHSV) of 19100 h<sup>–1</sup> (50 cm<sup>3</sup> min<sup>–1</sup> of VOC + 50 cm<sup>3</sup> min<sup>–1</sup> of synthetic air) and a W/F value of 0.03 g h l<sup>–1</sup>. The catalytic reaction was started when the reaction temperature was stable at 100 °C. The temperature was then raised by 5 °C/min from 100 °C up to 350 °C. The gaseous mixtures were analyzed via CO/CO<sub>2</sub> NDIR analyzers (ABB). Each test was repeated three times to ensure the reproducibility of the obtained results: the maximum deviation from the mean value for the three tests was ±5 °C.

The conversion of VOCs into CO<sub>2</sub> was calculated as

$$\text{Conversion}(\%) = \frac{F_{\text{CO}_2}}{\nu F_{\text{VOC},\text{in}}} \times 100$$

in which  $F_{\text{VOC},\text{in}}$  is the inlet molar flow rate of VOC,  $F_{\text{CO}_2}$  is the outlet molar flow rate of CO<sub>2</sub> in steady-state conditions and  $\nu$  is the number of carbon atoms in the VOC (for ethylene, propylene, toluene and mixture = 2, 3, 7 and 12, respectively).

Moreover, particular attention was devoted to determination of the C balance, which was found to always fall between 98% and 100% (calculated as the comparison between converted VOC and the CO<sub>2</sub> yield).

The catalytic activity of the catalytic monolith was conducted in a stainless steel reactor heated in a horizontal split tube furnace with a heating length of 60 cm. The catalyzed monolith was sandwiched between two mullite foams, in order to optimize the flow distribution. The inlet monolith temperature was controlled by inserting a thermocouple along one side of the central monolith channels. The inlet feed (1000 ppm mixture of ethylene, propylene and toluene, 10 vol.% O<sub>2</sub>, N<sub>2</sub> = balance) was controlled by means of mass-flow controllers. The catalyzed monolith was pre-treated in helium (flow rate = 100 cm<sup>3</sup> min<sup>−1</sup>) for 2 h at 100 °C to remove any species adsorbed on the catalyst surface. The reactor temperature difference, measured between the inlet and the outlet of the reactor in the axial direction, was not very significant (<15 °C). The composition of the outlet gases was monitored with the same equipment described above using three different GHSV (namely 9500, 19,100 and 38,000 h<sup>−1</sup>). In order to compare the catalytic performances of both catalytic monolith and powder Mn<sub>3</sub>O<sub>4</sub> at the same GHSV (=19,100 h<sup>−1</sup>), the W/F value was kept at 0.03 g h l<sup>−1</sup>.

### 3. Result and discussion

#### 3.1. Material textural properties

Table 2 shows the main textural properties of all the samples, derived from both the XRD patterns of the powder and N<sub>2</sub> physisorption isotherms.

Fig. 1 reports the XRD patterns of the prepared catalysts. The diffraction peaks of the Mn<sub>2</sub>O<sub>3</sub> crystalline phase (alpha) are present in the Mn<sub>2</sub>O<sub>3</sub> sample (curve a), while the peaks of the Mn<sub>3</sub>O<sub>4</sub> phase (hausmanite) are only observed for the Mn<sub>3</sub>O<sub>4</sub> catalyst (curve b). Moreover, the same Mn<sub>3</sub>O<sub>4</sub> phase can be observed for the monolithic catalyst (dotted line). No additional peaks can be seen, thus indicating the presence of a single crystalline phase in these catalysts. Conversely, two different crystalline phases are present in the Mn<sub>x</sub>O<sub>y</sub> catalyst (curve c), namely, the Mn<sub>2</sub>O<sub>3</sub> and MnO<sub>2</sub> phases [21]. The rather broad XRD peaks that can be observed suggest the occurrence of small crystallites with an average size of about 20 nm in the three samples, calculated according to the Scherrer equation.

Similar BET surface areas and total porous volumes were obtained with the prepared catalysts ( $S_{\text{BET}}$  = 43–47 m<sup>2</sup> g<sup>−1</sup>;  $V_p$  = 0.13–0.14 cm<sup>3</sup> g<sup>−1</sup>), thus allowing a reliable catalytic comparison to be made of the three prepared catalysts. Slightly larger

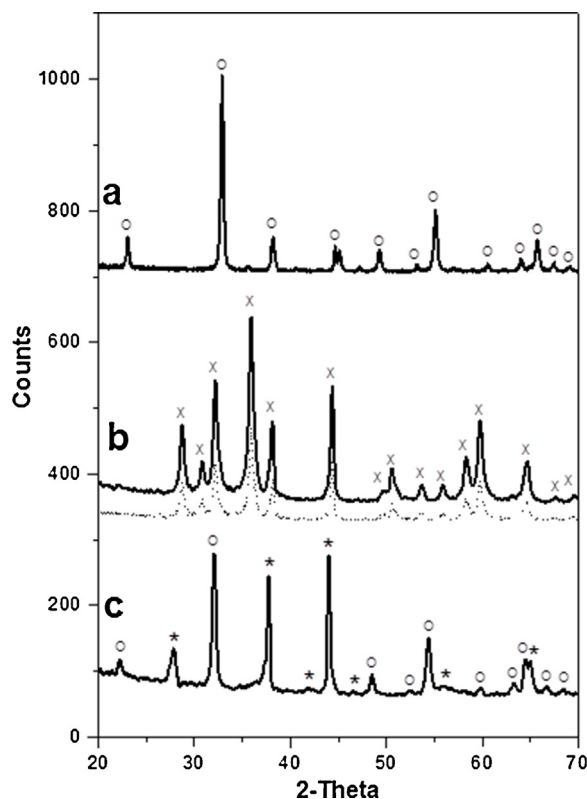


Fig. 1. Powder XRD patterns of the (a) Mn<sub>2</sub>O<sub>3</sub>, (b) Mn<sub>3</sub>O<sub>4</sub> and (c) Mn<sub>x</sub>O<sub>y</sub> samples. Dotted line: Mn<sub>3</sub>O<sub>4</sub>-based catalytic monolith. Assignments: Mn<sub>2</sub>O<sub>3</sub> peaks = O; Mn<sub>3</sub>O<sub>4</sub> peaks = X; MnO<sub>2</sub> peaks = asterisk.

pores sizes, due to the three-dimensional self-assembled nanoparticles, were attained for both Mn<sub>2</sub>O<sub>3</sub> and Mn<sub>3</sub>O<sub>4</sub> (ca. 20 nm) that for the Mn<sub>x</sub>O<sub>y</sub> sample (ca. 11 nm). However, the pore size, of all the prepared catalysts is likely related to interparticle voids rather than to intraparticle porosity and the contribute of the micropore volume is very low ( $V_{\text{micro}}$  = 0.01–0.02 cm<sup>3</sup> g<sup>−1</sup>).

The measured pore diameters ( $D_p$ ) are in fact in agreement with the cavities determined by the FE-SEM micrographies (Fig. 2, images a–c), which feature a 3-D network with ultra-large voids (ca. 20–50 nm in diameter). The latter should allow molecular diffusion along each direction in the catalytic framework.

It should be noted that these mesoporous structures were preserved in the catalyst pellets (250–450 μm in size) even after the reaction. In fact, as shown in Fig. 2 (images d–f), an array of 3-D mesoporous networks was maintained after catalytic combustion of the mixture of VOCs ( $T$  = 350 °C; TOS = 2 h), reflecting the good structural stability of the materials.

#### 3.2. Temperature-programmed studies

The TPD-O<sub>2</sub> profiles of all the prepared catalysts are shown in Fig. 3. The O<sub>2</sub> pattern of Mn<sub>2</sub>O<sub>3</sub> (curve a) is characterized by

Table 2

Textural properties of the samples, as derived from the XRD and N<sub>2</sub> isotherms at −196 °C.

Catalyst	Crystallites size <sup>a</sup> (nm)	$S_{\text{BET}}$ (m <sup>2</sup> g <sup>−1</sup> )	$V_p^b$ (cm <sup>3</sup> g <sup>−1</sup> )	$V_{\text{micro}}^c$ (cm <sup>3</sup> g <sup>−1</sup> )	$D_p^d$ (nm)
Mn <sub>2</sub> O <sub>3</sub>	21 ± 4	43	0.14	0.01	20
Mn <sub>3</sub> O <sub>4</sub>	17 ± 3	46	0.13	0.02	20
Mn <sub>x</sub> O <sub>y</sub>	19 ± 3 (Mn <sub>2</sub> O <sub>3</sub> ) 23 ± 4 (MnO <sub>2</sub> )	47	0.13	0.01	11

<sup>a</sup> Calculated applying the Scherrer formula.

<sup>b</sup>  $V_p$  = total pore volume.

<sup>c</sup>  $V_{\text{micro}}$  = micropore volume, measured according to  $t$ -plot method.

<sup>d</sup>  $D_p$  = pore diameter calculated according to the DFT method.

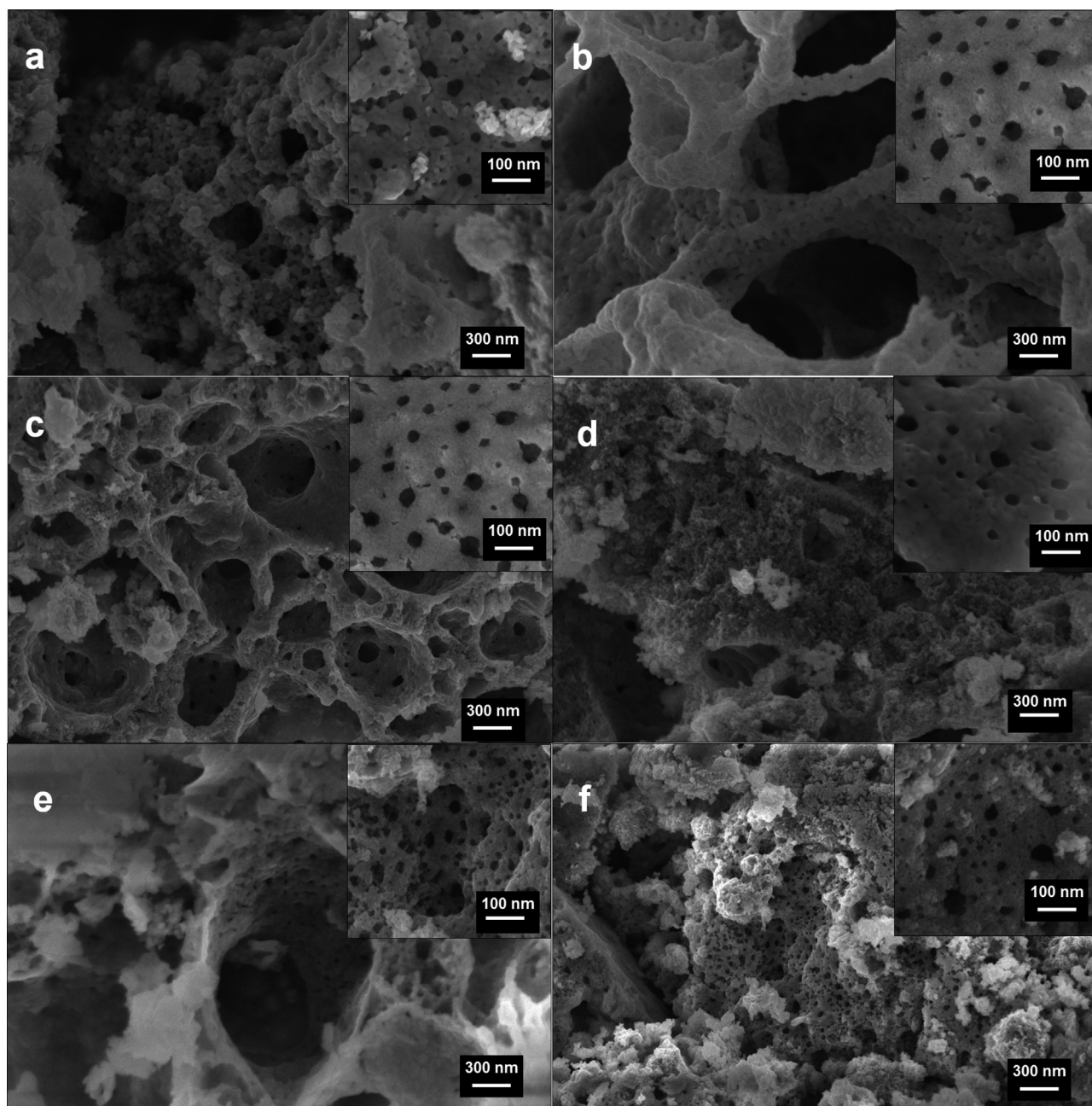


**Fig. 2.** Representative FESEM images of fresh (a)  $\text{Mn}_2\text{O}_3$ , (b)  $\text{Mn}_3\text{O}_4$  and  $\text{Mn}_x\text{O}_y$  (c) powders; FESEM images of the (d)  $\text{Mn}_2\text{O}_3$ , (e)  $\text{Mn}_3\text{O}_4$  and (f)  $\text{Mn}_x\text{O}_y$  pellets after reaction with the VOC mixture at 350 °C for 2 h.

two main peaks, at 840 and 870 °C, which can be ascribed to the reduction of  $\text{Mn}_2\text{O}_3$  to  $\text{Mn}_3\text{O}_4$  [15]. This behavior suggests that this sample has a different Mn–O bond strength and that the oxygen release results from the desorption of lattice oxygens ( $\beta$ -species).

The oxygen spectrum of  $\text{Mn}_3\text{O}_4$  (curve b) is more complex: (i) the weak signal at low temperature (350–450 °C) is due to chemisorbed oxygen ( $\text{O}^-$  and  $\text{O}_2^-$ ,  $\alpha$ -species) [26]; (ii) a main peak centered at 605 °C and the shoulder ca. 800 °C, can be attributed to structural oxygens ( $\beta$ -species) bound to lower and higher manganese oxidation states, respectively [15,16]. The  $\text{Mn}_3\text{O}_4$  phase in fact shows a spinel structure with  $\text{Mn}^{2+}$  ions in tetrahedral coordination and  $\text{Mn}^{3+}$  in tetragonally distorted octahedral sites [21]. It should be noted that most of the oxygen species (ca. 78% of the oxygen released during TPD analysis) can be ascribed to labile  $\beta$ -species, as reflected by the oxygen desorbed in the intermediate

temperature regions (450–650 °C). The  $\text{O}_2$  profile of  $\text{Mn}_x\text{O}_y$  (curve c) shows a lower temperature peak (centered at 535 °C), which can be ascribed to the reduction of  $\text{MnO}_2$  to  $\text{Mn}_2\text{O}_3$  (desorption of the labile  $\beta$ -species), whereas the peak at higher temperature regions (centered at 890 °C) corresponds to the reduction of  $\text{Mn}_2\text{O}_3$  [15]. These findings were supported by the XRD analysis (see above) which shows the presence of both the  $\text{MnO}_2$  and  $\text{Mn}_2\text{O}_3$  phases.

The reactivity of the oxygen species was investigated by means of  $\text{H}_2$ -TPR analysis. According to the literature [38,39], the reduction of manganese oxides can be described by the following steps:  $\text{MnO}_2 \rightarrow \text{Mn}_2\text{O}_3 \rightarrow \text{Mn}_3\text{O}_4 \rightarrow \text{MnO}$ . However, the TPR profiles could also depend on the Mn cations located in different environments [40]. Fig. 4 shows the  $\text{H}_2$ -TPR profiles of the fresh manganese oxide catalysts. For the  $\text{Mn}_2\text{O}_3$  sample (curve a), there is a reduction peak at 365 °C ( $\text{Mn}_2\text{O}_3 \rightarrow \text{Mn}_3\text{O}_4$ ) with a

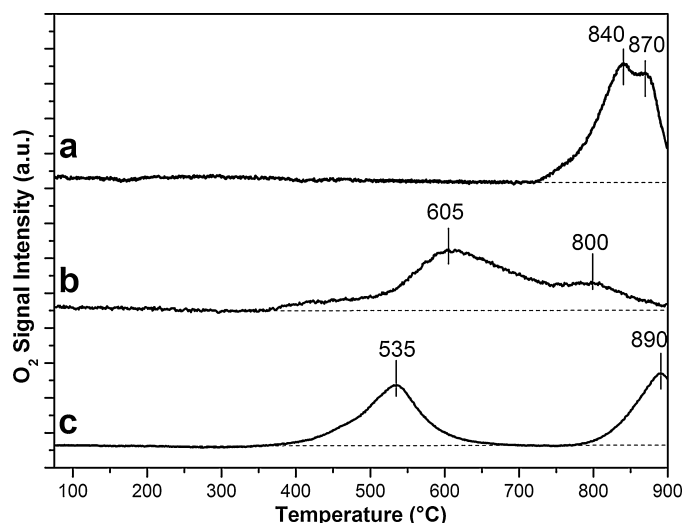


Fig. 3. O<sub>2</sub>-TPD profiles of the (a) Mn<sub>2</sub>O<sub>3</sub>, (b) Mn<sub>3</sub>O<sub>4</sub> and (c) Mn<sub>x</sub>O<sub>y</sub> samples.

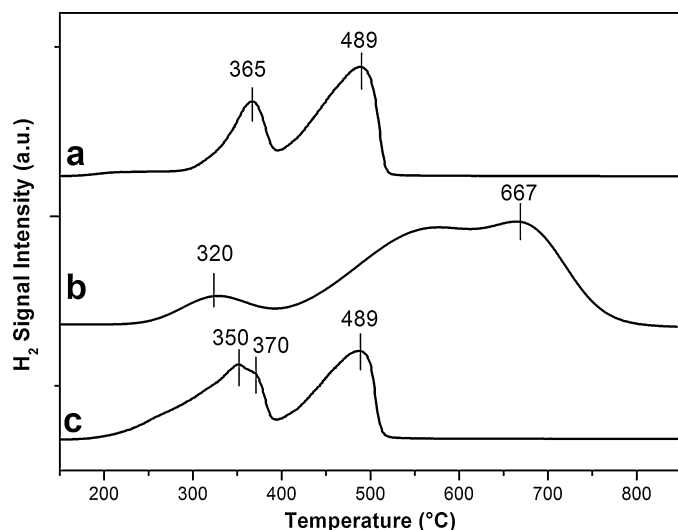


Fig. 4. H<sub>2</sub>-TPR profiles of the (a) Mn<sub>2</sub>O<sub>3</sub>, (b) Mn<sub>3</sub>O<sub>4</sub> and (c) Mn<sub>x</sub>O<sub>y</sub> samples.

shoulder peak at 489 °C (Mn<sub>3</sub>O<sub>4</sub> → MnO). The total H<sub>2</sub> consumption is 7.01 mmol g<sup>−1</sup>, which is in agreement with the theoretical H<sub>2</sub> consumption for the reduction of Mn<sub>2</sub>O<sub>3</sub> to MnO (=6.30 mmol g<sup>−1</sup>) [41].

The TPR profile of the Mn<sub>3</sub>O<sub>4</sub> sample (curve b) shows a low-temperature peak around 320 °C, which can be attributed to the reduction of Mn<sup>3+</sup> ions located in the tetrahedral sites of the hausmannite lattice [42], and a wide signal in the 500–700 °C temperature range, due to the hausmannite reduction (Mn<sub>3</sub>O<sub>4</sub> → MnO). Since MnO is the final reduction product (terminating at ca. 700 °C), the two peaks should reveal the reduction of two different Mn<sup>3+</sup>–O bonds (to MnO) that are available in Mn<sub>3</sub>O<sub>4</sub> [43]. The H<sub>2</sub> consumption (3.26 mmol g<sup>−1</sup>), related to the Mn<sub>3</sub>O<sub>4</sub> → MnO step, is in close agreement with the results found in the literature [26].

Table 4

Results of curve-fittings on the Mn2p<sub>3/2</sub> peaks in XP spectra of the catalysts: the maximum position (eV) is reported along with the corresponding atomic percentage for Mn<sup>4+</sup>, Mn<sup>3+</sup> and Mn<sup>2+</sup> ions.

Sample	Mn <sup>4+</sup> (% atom)	Mn <sup>4+</sup> BE (eV)	Mn <sup>3+</sup> (% atom)	Mn <sup>3+</sup> BE (eV)	Mn <sup>2+</sup> (% atom)	Mn <sup>2+</sup> BE (eV)	Mn <sup>4+</sup> /Mn <sup>3+</sup>	Mn <sup>3+</sup> /Mn <sup>2+</sup>
Mn <sub>2</sub> O <sub>3</sub>	33.4	643.3	52.8	641.9	13.8	640.9	0.63	3.82
Mn <sub>3</sub> O <sub>4</sub>	28.0	643.3	50.1	641.9	22.0	640.7	0.56	2.27
Mn <sub>x</sub> O <sub>y</sub>	48.5	643.7	37.9	642.3	13.6	641.0	1.28	2.78

Table 3

Results of curve-fittings on the O 1s binding energies of the catalysts. The relative ratios of surface-adsorbed oxygen (O<sub>α</sub>) and lattice oxygen (O<sub>β</sub>) are reported in the last column.

Sample	O <sub>α</sub> (% atom)	O <sub>α</sub> BE (eV)	O <sub>β</sub> (% atom)	O <sub>β</sub> BE (eV)	O <sub>α</sub> /O <sub>β</sub>
Mn <sub>2</sub> O <sub>3</sub>	24.0	531.3	76.0	529.7	0.32
Mn <sub>3</sub> O <sub>4</sub>	27.2	531.7	72.8	530.1	0.37
Mn <sub>x</sub> O <sub>y</sub>	20.2	531.1	79.8	529.7	0.25

In the case of the Mn<sub>x</sub>O<sub>y</sub> sample (curve c), two reduction peaks appear at 350 °C and 370 °C: the former is due to the reduction of MnO<sub>2</sub> (MnO<sub>2</sub> → Mn<sub>2</sub>O<sub>3</sub>) and the latter can be assigned to the reduction of Mn<sub>2</sub>O<sub>3</sub> (Mn<sub>2</sub>O<sub>3</sub> → Mn<sub>3</sub>O<sub>4</sub>). The main peak at 489 °C can in fact be attributed to the reduction of Mn<sub>3</sub>O<sub>4</sub>. This sample exhibits a comparable H<sub>2</sub> consumption to that of the Mn<sub>2</sub>O<sub>3</sub> catalyst (=7.82 mmol g<sup>−1</sup>), and the presence of two crystalline phases (Mn<sub>2</sub>O<sub>3</sub> and MnO<sub>2</sub>) does not seem to improve the mobility of the electrons or lattice oxygen inside the solid.

### 3.3. Spectroscopic characterization of the surface functionalities

#### 3.3.1. X-ray photoelectron spectroscopy

Fig. 5 reports the XPS spectra in the O 1s and Mn 2p BE regions. The O 1s spectra reported in Fig. 5A present different features, which depend on both the chemisorbed oxygen species (O<sub>α</sub>) and the lattice oxygen (O<sub>β</sub>). As a whole, the peak at 529.7–530.1 eV corresponds to O<sub>β</sub> (O<sup>2−</sup>), whereas the signal at 531.1–531.7 eV can be attributed to surface-adsorbed oxygen species (i.e. O<sub>2</sub><sup>2−</sup>, O<sup>−</sup>, OH<sup>−</sup>, CO<sub>3</sub><sup>2−</sup>) [44,45]. The latter have greater mobility than lattice oxygen and may give rise to beneficial spillover phenomena at the solid surface [21].

As reported in Table 3, the highest O<sub>α</sub>/O<sub>β</sub> ratio is attained for the Mn<sub>3</sub>O<sub>4</sub> sample, thus confirming a large amount of surface adsorbed oxygen species, as observed by means of O<sub>2</sub>-TPD analysis. It is worth noting that the lattice O<sup>2−</sup> ions are nucleophilic reagents and are usually responsible for selective oxidation reactions. Conversely electrophilic oxygens (O<sub>2</sub><sup>−2</sup>, O<sup>−</sup> and O<sub>2</sub><sup>−</sup>), which implies the formation of radicals, are highly reactive and give rise to total oxidations [34,46,47]. Fig. 5A shows the Mn 2p XPS spectra of the samples in the 635–660 eV range. The binding energies at the 640.0–650.0 eV and 650.0–660.0 eV regions can be attributed to Mn 2p<sub>3/2</sub> and Mn 2p<sub>1/2</sub>, respectively [48–50]. The relative abundance of the surface Mn<sup>2+</sup>, Mn<sup>3+</sup> and Mn<sup>4+</sup> species for each sample was calculated by considering the deconvolution of Mn 2p 3/2 [16,44,46,47]. As expected, the lowest Mn<sup>4+</sup>/Mn<sup>3+</sup> and Mn<sup>3+</sup>/Mn<sup>2+</sup> ratios were obtained for the Mn<sub>3</sub>O<sub>4</sub> catalyst. Conversely, the highest Mn<sup>4+</sup>/Mn<sup>3+</sup> ratio was observed for the Mn<sub>x</sub>O<sub>y</sub> sample, due to the co-presence of the MnO<sub>2</sub> and Mn<sub>2</sub>O<sub>3</sub> phases, whereas the Mn<sub>2</sub>O<sub>3</sub> sample exhibited the maximum Mn<sup>3+</sup>/Mn<sup>2+</sup> ratio value. These results are in fair agreement with the crystalline phases obtained by means of XRD analysis (Table 4).

#### 3.3.2. Infrared spectroscopy via ammonia adsorption at r.t.

Fig. 6 shows the spectra of samples outgassed at 150 °C before the adsorption experiments. All the reported spectra were normalized to unit specific weight to allow a comparison to be made. As a whole, the IR spectra of the prepared samples show

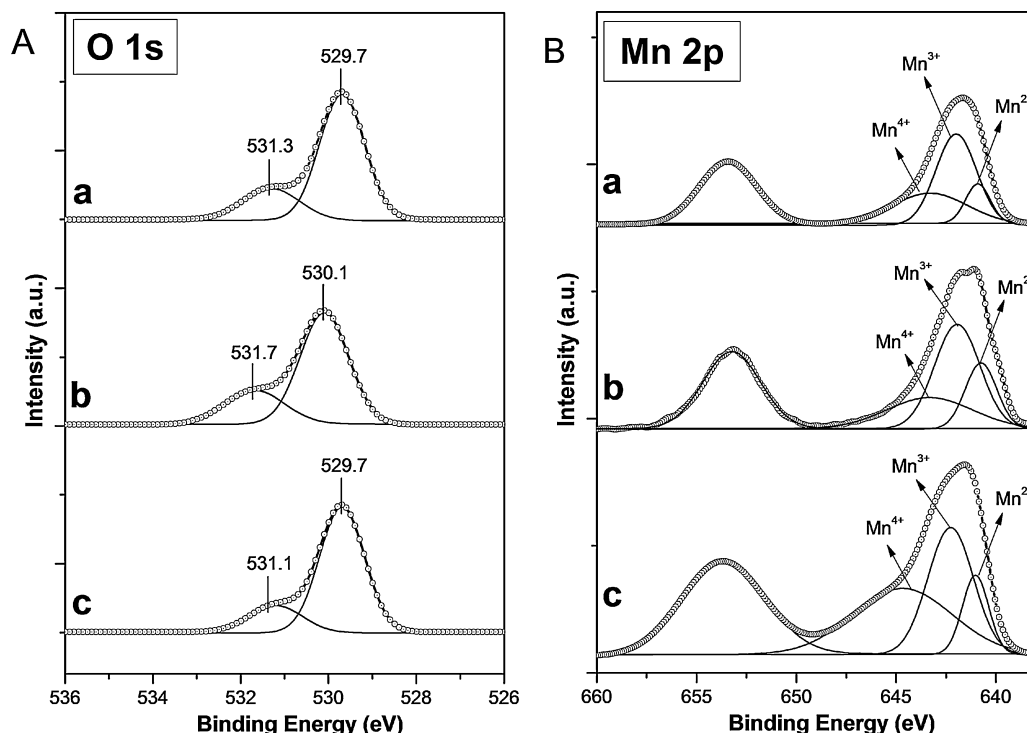


Fig. 5. XPS spectra of the (a)  $\text{Mn}_2\text{O}_3$ , (b)  $\text{Mn}_3\text{O}_4$  and (c)  $\text{Mn}_x\text{O}_y$  samples in the Mn (2p) (Section A) and O (1s) core level regions (Section B).

several adsorptions in the  $3800\text{--}3000\text{ cm}^{-1}$  region, where the O–H stretching modes fall. The formation of a coordination bond on the ionic oxides, such as manganese oxides, decreases the frequency of the OH stretching vibrations: the stretching is higher for the terminal OH groups, intermediate for the bridging OH's and lower for the triply bridging OH's [51]. Isolated OH stretching bands are found in the  $\text{Mn}_3\text{O}_4$  spectrum at  $3747\text{ cm}^{-1}$  (curve b) while for  $\text{Mn}_2\text{O}_3$  (curve a) and  $\text{Mn}_x\text{O}_y$  (curve c) only bridging OH groups are detected in the region between  $3600$  and  $3300\text{ cm}^{-1}$ . Signals in the  $1600\text{--}1300$  region are assigned to surface carbonate species, whereas the strong peak at  $2338\text{ cm}^{-1}$  is due to trapped  $\text{CO}_2$  (the latter band only appears for  $\text{Mn}_3\text{O}_4$ ) [52]. When acting as an electrophile,  $\text{CO}_2$  reacts with oxygen defects or hydroxide species and gives rise to carbonate or bicarbonate species, which are both particularly abundant on the  $\text{Mn}_3\text{O}_4$  surface.

The surface acidity was studied by means of ammonia adsorption at room temperature: Ammonia is probably the most frequently used probe molecule for the acidity assessment of solid catalysts, because it can interact with both Brønsted acidic sites (by forming ammonium ions) and Lewis acidic sites (by forming acidic–basic adducts) [53]. Negative and positive bands correspond therefore to species disappearing and appearing after ammonia dosage, respectively. Its relatively small size allows quantitative probing of almost all acid sites in micro-, meso- and macro-porous oxides [54]. The protonated species ( $\text{NH}_4^+$  ions) and the coordinatively bonded  $\text{NH}_3$  differ, from a spectroscopic point of view, both in terms of NH deformations and stretching vibrations.

$\text{NH}_4^+$  shows typical absorptions at ca.  $1450$  and  $3300\text{ cm}^{-1}$ , whereas co-ordinatively bonded  $\text{NH}_3$  molecules absorb at ca.  $1250$ ,  $1630$  and  $3330\text{ cm}^{-1}$ . The deformation vibrations (bending modes) at  $1450$  and  $1630\text{ cm}^{-1}$  provide reliable indicators of the presence of protonated and coordinatively bonded ammonia, respectively [54].

Fig. 7 shows the difference IR spectra of samples outgassed at  $150^\circ\text{C}$ , obtained by subtracting those of bare samples (reported in Fig. 6), recorded after dosing ca. 2 mbar of  $\text{NH}_3$ . Three negative bands can be seen in the OH stretch range (Fig. 7A) at  $3740$ ,  $3650$  and  $3606\text{ cm}^{-1}$ , and a broad absorption, with a maximum at about  $3300\text{ cm}^{-1}$ , can be seen for the  $\text{Mn}_3\text{O}_4$  sample (curve b). These features can be attributed to the presence of different types of hydroxyl groups (isolated, H-bonded and defective Mn–OH, respectively) which interact with  $\text{NH}_3$  via the formation of H-bonding [55–57]. The presence of atomic-like defects (nanodefects or microcavities) is probably responsible for the anomalous abundance of OH groups on the  $\text{Mn}_3\text{O}_4$  sample, while the signal at  $3606\text{ cm}^{-1}$  was previously assigned to defective –OH groups in other transition metal oxides [13,58,59].

In agreement with the Volkenshtein Electronic Theory [60,61], the presence of structural defects, associated with oxygen vacancies, modifies the Fermi Energy level and hence may favor oxidation reactions. Two negative bands appear at  $3730$  and  $3626\text{ cm}^{-1}$  for both  $\text{Mn}_2\text{O}_3$  (curve a) and  $\text{Mn}_x\text{O}_y$  (curve c). The former sample

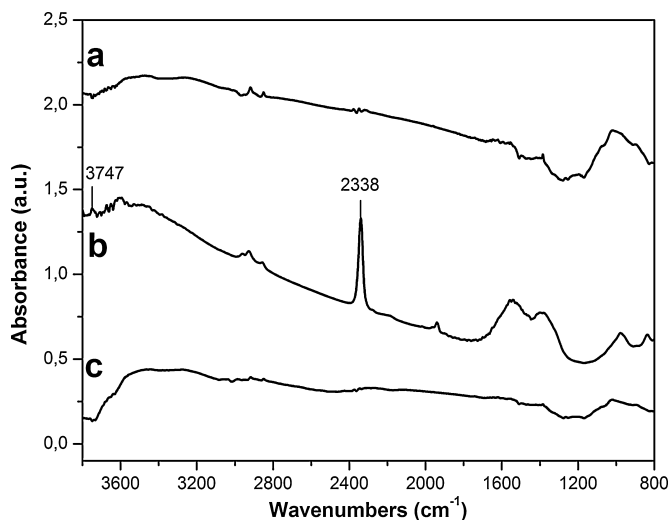
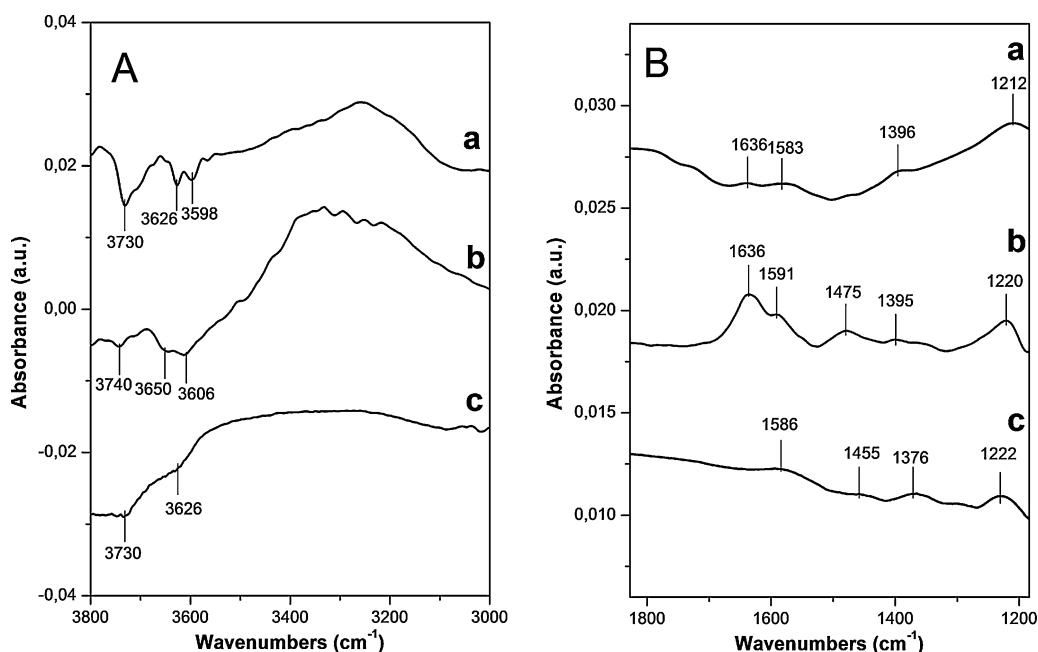


Fig. 6. Normalized FT-IR spectra of the (a)  $\text{Mn}_2\text{O}_3$ , (b)  $\text{Mn}_3\text{O}_4$  and (c)  $\text{Mn}_x\text{O}_y$  samples outgassed at  $150^\circ\text{C}$ .



**Fig. 7.** FT-IR difference spectra recorded after dosing at room temperature ca. 2 mbar of  $\text{NH}_3$  on samples outgassed at  $150^\circ\text{C}$ . (A) OH stretch region ( $3800\text{--}3000\text{ cm}^{-1}$ ); (B) N–H bending region. Curve a:  $\text{Mn}_2\text{O}_3$  sample ( $p\text{ NH}_3 = 1.7\text{ mbar}$ ); curve b:  $\text{Mn}_3\text{O}_4$  sample ( $p\text{ NH}_3 = 1.8\text{ mbar}$ ); curve c:  $\text{Mn}_x\text{O}_y$  sample ( $p\text{ NH}_3 = 1.8\text{ mbar}$ ).

exhibits a further (weak) signal at  $3598\text{ cm}^{-1}$ , which is likely due to the presence of a few defective OH species.

Fig. 7B reports the same spectra in the NH bending mode region ( $1830\text{--}1180\text{ cm}^{-1}$ ). As reported in literature, the bands at  $1620\text{--}1590\text{ cm}^{-1}$  (asymmetric deformation vibration,  $\delta_{\text{as}}$ ) and  $1230\text{--}1210\text{ cm}^{-1}$  (symmetric deformation vibration,  $\delta_{\text{s}}$ ) can be attributed to  $\text{NH}_3$  molecules adsorbed on Mn sites, acting as Lewis acid centers [51,55–57]. Such signals are particularly intense for the  $\text{Mn}_3\text{O}_4$  sample, suggesting a large presence of coordinatively unsaturated Mn cations on the surface [51,55]. Instead, fewer Lewis acid sites appear on the surface of both the  $\text{Mn}_2\text{O}_3$  and  $\text{Mn}_x\text{O}_y$  catalysts.

Moreover, the adsorption bands corresponding to the Brønsted acid sites ( $\delta_{\text{as}}\text{ NH}_4^+$  at  $1395$  and  $1475\text{ cm}^{-1}$  and one maximum at  $1636\text{ cm}^{-1}$  [51,55–57]) are more intense on  $\text{Mn}_3\text{O}_4$  than those recorded on  $\text{Mn}_2\text{O}_3$  or  $\text{Mn}_x\text{O}_y$ , thus indicating a higher abundance of Brønsted hydroxyls (Mn–OH groups). The latter species can easily be converted into Lewis acidic sites by dehydroxylation and can thus play a key role on the catalytic activity at higher temperatures. Dehydroxylated oxide surfaces can in fact be considered as a spatially organized distribution of charged ions, such as  $\text{Mn}^{n+}\text{O}^{2-}\text{Mn}^{n+}\text{O}^{2-}\text{Mn}^{n+}$ ; however, the interaction of water with such oxide surfaces is in part dissociative so that coordinatively unsaturated Mn ions, performing as Lewis acidic sites, convert into hydroxyl-groups (Mn–O $^{\delta-}$ –H $^{\delta+}$ ).

### 3.4. Catalytic activity tests

#### 3.4.1. Total VOC oxidation on the powder catalysts

The catalytic behavior towards VOC decomposition was tested in the  $100\text{--}350^\circ\text{C}$  temperature range. Fig. 8A reports the ethylene conversion as a function of temperature: as expected, ethylene shows no conversion in the absence of the catalyst in this temperature range (i.e. 10% ethylene conversion was obtained at  $720^\circ\text{C}$ ), whereas all the prepared catalysts display positive ethylene conversion trends for an increasing reaction temperature. However, different conversion values can be observed: complete oxidation to  $\text{CO}_2$  occurs at  $260\text{--}265^\circ\text{C}$  for the  $\text{Mn}_3\text{O}_4$  catalyst, whereas  $\text{Mn}_2\text{O}_3$  shows a lower activity, since the temperature for

complete oxidation into  $\text{CO}_2$  is at  $330\text{--}335^\circ\text{C}$ ; the lowest ethylene conversion is achieved for  $\text{Mn}_x\text{O}_y$  (i.e. 92% conversion at  $350^\circ\text{C}$ ). These results are in fair agreement with previous studies on manganese oxide catalysts that are effective towards the oxidation of VOCs and following a redox-type mechanism [26,62].

Similar catalytic behavior was observed for propylene (Fig. 8B) and toluene (Fig. 8C) total oxidations, although higher conversion values were achieved for both reactions, likely due to the higher adsorption capacity of these compounds on surfaces [63]. Like to the results obtained for ethylene oxidation, with either propylene or toluene molecules, the following reactivity trend was observed:  $\text{Mn}_3\text{O}_4 > \text{Mn}_2\text{O}_3 > \text{Mn}_x\text{O}_y$ . However, a better discrimination of the catalytic activity of the prepared catalysts was obtained with ethylene as the probe molecule.

The catalytic conversions of the VOC mixture (ethylene, propylene and toluene) over the prepared catalysts are reported in Fig. 8D. Again in this case,  $\text{Mn}_3\text{O}_4$  is the most active catalyst and this is followed by  $\text{Mn}_2\text{O}_3$  and  $\text{Mn}_x\text{O}_y$ . Note, the XRD analysis of the used catalysts (recorded after reaction with the VOC mixture;  $T = 350^\circ\text{C}$ ,  $\text{TOS} = 2\text{ h}$ ), revealed that the crystalline phases of the catalysts are still preserved (data not reported for the sake of brevity).

The conversion values are comparable with those obtained using toluene, likely due to the fact that the latter molecule shows the highest adsorbance capacity on the catalyst surface. Therefore, the best performances were achieved with  $\text{Mn}_3\text{O}_4$ , which showed the highest amount of adsorbed oxygen ( $\alpha$ -species), probably due to the presence of various surface defects (i.e. kinks, steps, corners, etc.). In fact, FT-IR spectroscopy by means of  $\text{NH}_3$  adsorption at r.t., revealed a high number of Brønsted acidic sites on the hydrated  $\text{Mn}_3\text{O}_4$  and of the corresponding Lewis acidic sites on the dehydroxylated  $\text{Mn}_3\text{O}_4$ .

These acidic properties are very important in oxidation catalysis, since the surface acidity, as well as the basic properties, may be responsible for the adsorption/desorption rates of reactants and products, and are a major factor in the activation of hydrocarbons and occurring intermediates [30].

On the other hand, it is known that surface oxygen species play a key role on catalytic activity in oxidation reactions, especially

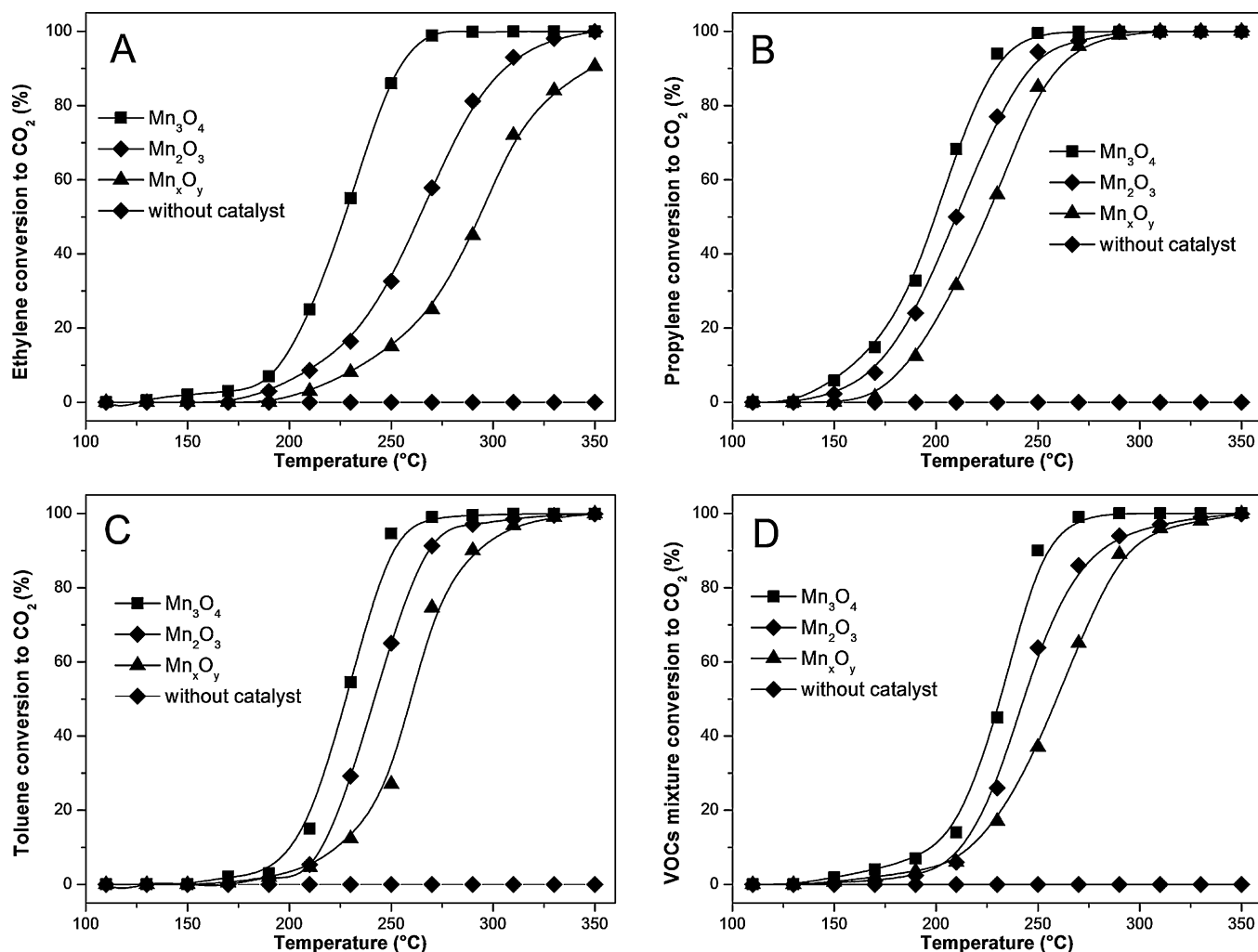


Fig. 8. Catalytic results of powder catalysts for the total oxidation of (a) ethylene, (b) propylene, (c) toluene and (d) VOC mixture (ethylene, propylene and toluene) as a function of the reaction temperature.

at temperatures below 400 °C [62]. At low temperatures, only the outer catalyst layer may be equilibrated with oxygen in the gas-phase; at temperatures high enough, instead, surface defects diffuse into the bulk and an equilibrium is obtained between the gas-phase and the solid oxide. Hence, oxidation reaction mechanisms on solid catalysts may adapt as a function of temperature [64]. G.I. Golodets [65] proposed an overall classification of oxidation mechanisms as a function of temperature, according to which surface redox-cycles (MvK-type mechanism) occur at moderate temperatures (300–500 °C), and are replaced at higher temperatures by radical processes in the gas-phase. He also identified a “transitional” region between 100–300 °C, in which complex surface oxidation/re-oxidation mechanisms (i.e. oxygen spillover phenomena) take place; the latter is probably responsible for the formation of the total oxidation products. Similarly, according to Boreskov’s classification [66], oxidation reactions occur via an associative (concerted) or redox (step-wise) mechanism: the former is characterized by lower activation energies, whereas the latter involves lattice oxygen and displays higher activation energies. The occurrence of one or other of the two mechanisms depends above all on the oxygen storage capacity (OSC) and lattice oxygen availability of the catalyst. In the present case, both the Mn<sub>2</sub>O<sub>3</sub> and Mn<sub>x</sub>O<sub>y</sub> catalysts displayed a lower amount of surface oxygen species than Mn<sub>3</sub>O<sub>4</sub>, suggesting the beneficial role of electrophilic oxygens (O<sub>α</sub>-species) towards VOC total oxidation, which is kinetically modeled

through a MvK-type mechanism over the 100–350 °C temperature range.

Fig. 9 shows the relationship between the O<sub>α</sub>/O<sub>β</sub> atomic ratios of the prepared catalysts and their performances, expressed in terms of temperature (°C), at which 10%, 50% and 90% ethylene conversion to CO<sub>2</sub> is obtained (T<sub>10</sub>, T<sub>50</sub> and T<sub>90</sub>, respectively). Similar correlations can be obtained with either propylene or toluene total oxidations (data not reported for the sake of brevity).

In order to analyze the stability of the most active catalyst, further experiments were conducted with ethylene oxidation on the Mn<sub>3</sub>O<sub>4</sub> sample. For instance, the conversion to CO<sub>2</sub> at 310 °C as a function of time-on-stream (TOS) is shown in Fig. 10. The conversion maintained an almost constant value for about 1 h, then a slight activity decrease occurred (ca. 7% over the next 6 h), likely due to an accumulation of reaction products on the catalyst surface, which blocked the active centers and favored their reduction. It seems reasonable, considering the MvK-type mechanism, that oxides with the highest metal oxidation state should exhibit the highest oxidation activity, since they have more oxygen atoms that can be used for the reaction [15]. However, the redox properties of Mn<sub>3</sub>O<sub>4</sub> can be readily restored by a pre-treatment in air at 100 °C for 20 min as was confirmed after several heating-cooling cycles. Fig. 11 shows the catalytic performances of the same catalyst, as a function of temperature, on each heating run and then kept at 350 °C for 2 h. Similar catalytic results were achieved during these

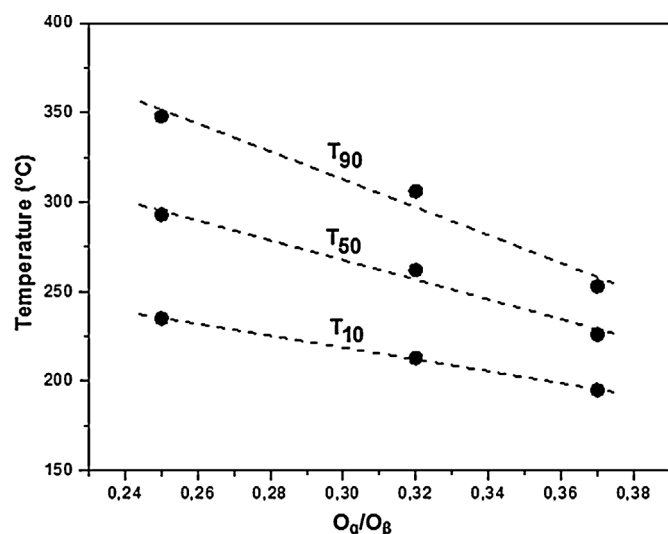


**Fig. 9.** Correlation between the  $O_{\alpha}/O_{\beta}$  ratios of the manganese oxide catalysts and their catalytic activity expressed in terms of temperature ( $^{\circ}\text{C}$ ) at which 10%, 50% and 90% ethylene conversions into  $\text{CO}_2$  are obtained ( $T_{10}$ ,  $T_{50}$  and  $T_{90}$ , respectively).

four cycles and no significant deactivation was observed in terms of total ethylene conversion.

### 3.4.2. VOC total oxidation by means of the $\text{Mn}_3\text{O}_4$ -based catalytic monolith

Since industrial emissions usually contain mixtures of VOCs, studies on the catalytic activity of a single probe molecule of VOC only partially represent the possible catalyst applications. Therefore, the catalytic behavior of the  $\text{Mn}_3\text{O}_4$ -monolithic catalyst (Fig. 12) was tested for the total oxidation of the VOC mixture using three different GHSV values. In order to be sure that the obtained VOC conversion was due to the catalytic process and not to the support or thermal decomposition, non-catalytic bare support material (not reported here) was also tested. However, no conversion was obtained for the temperature range in which catalytic conversion took place. As can be seen in Fig. 13, the  $\text{Mn}_3\text{O}_4$ -based monolith showed good catalytic performances for the total VOC oxidation, which are comparable to those obtained with the powder  $\text{Mn}_3\text{O}_4$  ( $T_{50}$  and  $T_{90}$  values are 231 and 262  $^{\circ}\text{C}$ , respectively;

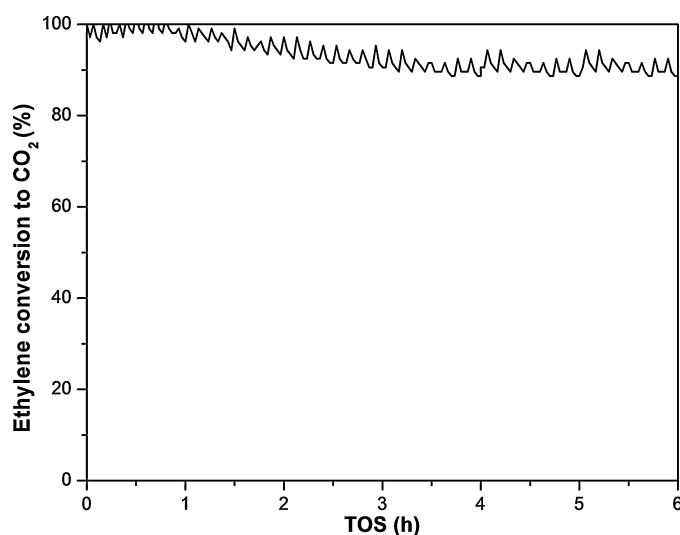


**Fig. 10.** Evolution of the conversion into  $\text{CO}_2$  with time-on-stream on the  $\text{Mn}_3\text{O}_4$  catalyst at 310  $^{\circ}\text{C}$ .

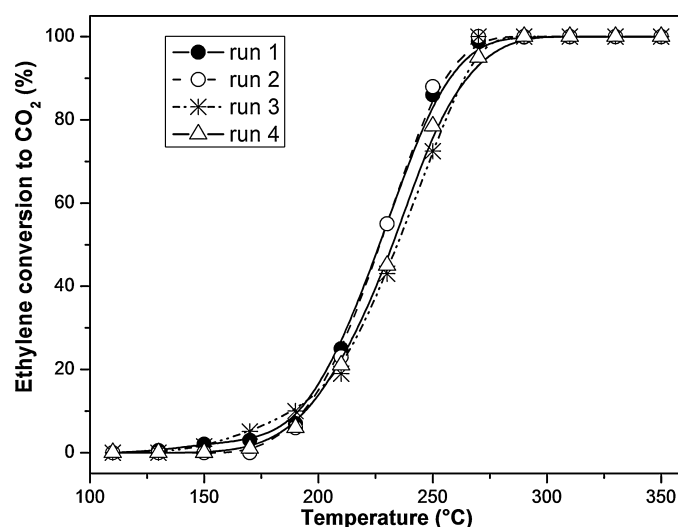


**Fig. 11.** Stability study of the  $\text{Mn}_3\text{O}_4$  catalyst for four successive ethylene oxidation runs.

with  $\text{GHSV} = 19,100 \text{ h}^{-1}$ ). However, better results were achieved at lower GHSV ( $9500 \text{ h}^{-1}$ ), since the reactant molecules ( $\text{O}_2$  and VOCs) are retained more within the pores, thus favoring total oxidation reactions. However, lower activities occurred at higher GHSV ( $38,000 \text{ h}^{-1}$ ) as a consequence of the lower residence time of the molecules in the catalyst framework.

Catalyst stability is an important criterion for catalysts in industrial applications; hence, a continuous supply of the VOC mixture was fed to the  $\text{Mn}_3\text{O}_4$ -based monolith catalyst for a TOS of 10 h at constant temperature (310  $^{\circ}\text{C}$ ) (Fig. 14). As a result, the catalyst showed excellent stability over the time span and no deactivation of the conversion values occurred during the reaction. Moreover, the monolithic catalyst was tested under alternating temperature conditions (namely at 410  $^{\circ}\text{C}$  and 245  $^{\circ}\text{C}$ , two cycles), thus showing no deactivation of the catalytic activity (Fig. 15). Therefore, these findings suggest the potential application of the  $\text{Mn}_3\text{O}_4$ -based catalytic monolith for VOCs removal in “harder” conditions.

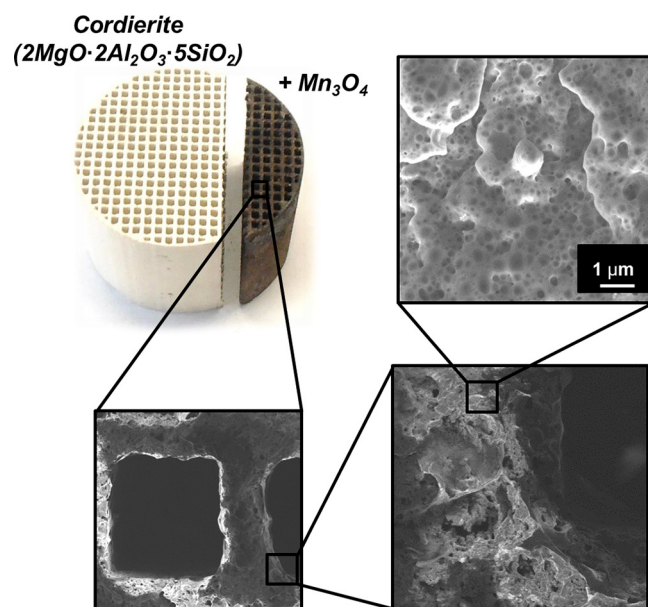


**Fig. 12.**  $\text{Mn}_3\text{O}_4$ -based monolith catalyst obtained by means of direct synthesis (via SCS route).

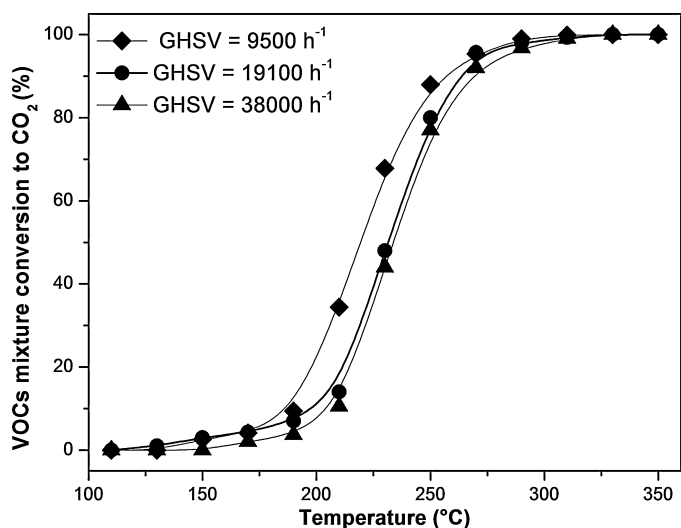


Fig. 13. Catalytic results of the Mn<sub>3</sub>O<sub>4</sub>-based monolith catalyst for the total oxidation of the VOC mixture (ethylene, propylene and toluene) at different gas hourly space velocities (GHSV) as a function of the reaction temperature.

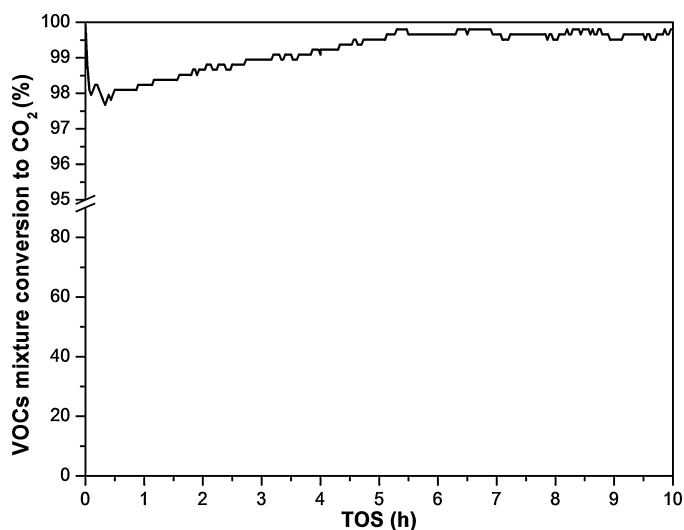


Fig. 14. Evolution of the conversion into CO<sub>2</sub> with time-on-stream of the Mn<sub>3</sub>O<sub>4</sub>-based monolith catalyst at 310 °C (GHSV = 19,100 h<sup>-1</sup>).

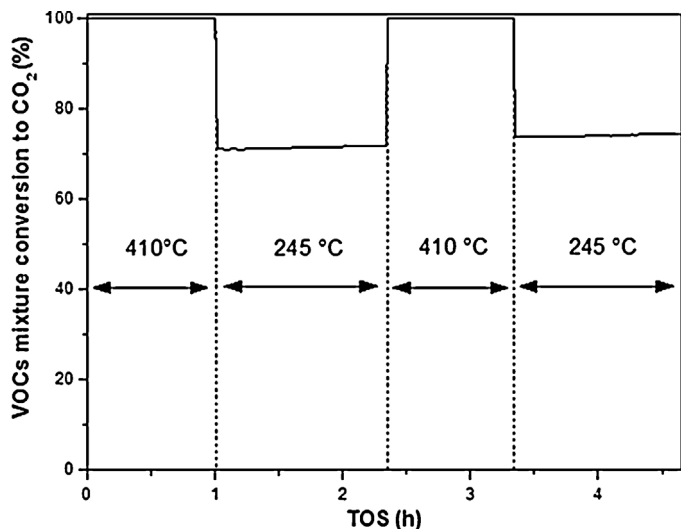


Fig. 15. Evolution of the conversion into CO<sub>2</sub> with time-on-stream of the Mn<sub>3</sub>O<sub>4</sub>-based monolith catalyst under alternating temperature conditions (GHSV = 19,100 h<sup>-1</sup>).

#### 4. Conclusions

A set of three mesoporous manganese oxide catalysts (Mn<sub>2</sub>O<sub>3</sub>, Mn<sub>3</sub>O<sub>4</sub> and Mn<sub>x</sub>O<sub>y</sub>) has been prepared by the SCS route, using different synthesis conditions, and tested for the total oxidation of VOCs (ethylene, propylene, toluene and their mixture). The best results for all the probe molecules, in terms of total VOC oxidation, were achieved for the Mn<sub>3</sub>O<sub>4</sub> catalyst, which showed the highest amount of electrophilic oxygens on the surface (O<sub>α</sub> species). The latter species are beneficial for the total oxidation of VOCs, kinetically modelled through an MvK-type mechanism. Moreover, FT-IR analysis has revealed an abundant population of Brønsted acidic sites (i.e. Mn–OH) on the hydrated Mn<sub>3</sub>O<sub>4</sub> catalyst, likely due to various structural defects and, as a result, corresponding uncoordinated Mn<sup>n+</sup> Lewis sites occur due to the dehydroxylation mechanism. These acidic features play a key role in oxidation catalysis, since the acidic sites, as well as the surface basicity, are responsible for the adsorption/desorption rates of the reactants and products, and are a major factor in the activation of hydrocarbons and intermediates that occur.

The most active powder catalyst (Mn<sub>3</sub>O<sub>4</sub>) was deposited on a cordierite-type monolith through a novel direct synthesis and tested for the total oxidation of the VOC mixture, using different GHSV values. Interestingly, the Mn<sub>3</sub>O<sub>4</sub>-based monolith exhibited high activity towards the total VOC oxidation, which was comparable with that obtained for the powder Mn<sub>3</sub>O<sub>4</sub>.

It should be noted that the monolithic catalyst exhibited excellent catalytic activity during the combustion of the mixture of VOCs (conversion to CO<sub>2</sub> = 99.2% ± 0.5) over a time-on-stream of 10 h at constant temperature (310 °C), and no deactivation occurred during the reaction. Contact between the reactant molecules and the Mn<sub>3</sub>O<sub>4</sub> active phase loaded onto the monolith is in fact ensured by the effective transport phenomena, and reversible (or nearly reversible) redox cycles may therefore occur. These features render manganese oxide-based catalysts suitable for practical applications.

#### Acknowledgments

The Ministero dell'Università e della Ricerca (MIUR) is acknowledged for sponsoring this research activity (FIRB–Futuro in Ricerca 2012). The authors would like to thank Dr. Micaela Castellino (DISAT, Politecnico di Torino) for the XPS measurements.

#### References

- [1] L.F. Liotta, *Appl. Catal. B* 100 (2010) 403–412.
- [2] G. Ertl, H. Knözinger, F. Schüth, J. Weitkamp, *Handbook of Heterogeneous Catalysis*, second ed., Weinheim, Wiley-VCH, 2008, pp. 2394–2411.
- [3] B.K. Hodnett, *Heterogeneous Catalytic Oxidation*, Wiley-VCH, New York, 2000, pp. 189–238.
- [4] S.H. Taylor, *Top. Catal.* 52 (2009) 457.
- [5] M. Hakim, Y.Y. Broza, O. Barash, N. Peled, M. Phillips, A. Amann, H. Haick, *Chem. Rev.* 112 (2012) 5949–5966.
- [6] R. Atkinson, *Atmos. Environ.* 34 (2000) 2063–2101.
- [7] R. Atkinson, J. Arey, *Chem. Rev.* 103 (2003) 4605–4638.
- [8] T. Mitsui, T. Matsui, R. Kikuchi, K. Eguchi, *Top. Catal.* 52 (2009) 465–469.
- [9] K. Everaert, J. Baeyens, *J. Hazard. Mater.* 109 (2004) 113–139.
- [10] C. Gennequin, S. Siffert, R. Cousin, A. Aboukais, *Top. Catal.* 52 (2009) 482–491.
- [11] L. Pinard, J. Mijoin, P. Magnoux, M. Guisnet, *J. Catal.* 215 (2003) 234–244.
- [12] H.L. Tidahy, S. Siffert, F. Wyrwalski, J.F. Lamonier, A. Abouka, *Catal. Today* 119 (2007) 317–320.
- [13] M. Piumetti, B. Bonelli, M. Armandi, L. Gaberova, S. Casale, P. Massiani, E. Garrone, *Microporous Mesoporous Mater.* 133 (2010) 36–44.
- [14] S.L. Brock, N.G. Duan, Z.R. Tian, O. Giraldo, H. Zhou, S.L. Suib, *Chem. Mater.* 10 (1998) 2619–2628.
- [15] V.P. Santos, M.F.R. Pereira, J.J.M. Órfão, J.L. Figueiredo, *Top. Catal.* 52 (2009) 470–481.
- [16] V.P. Santos, M.F.R. Pereira, J.J.M. Órfão, J.L. Figueiredo, *Appl. Catal. B* 99 (2010) 353–363.
- [17] J. Luo, Q. Zhang, A. Huang, S.L. Suib, *Microporous Mesoporous Mater.* 35–36 (2000) 209–217.

- [18] J. Cai, J. Liu, W.S. Willis, S.L. Suib, *Chem. Mater.* 13 (2001) 2413–2422.
- [19] J. Luo, Q. Zhang, J. Garcia-Martinez, S.L. Suib, *J. Am. Chem. Soc.* 130 (2008) 3198–3207.
- [20] V.P. Santos, M.F.R. Pereira, J.J.M. Órfão, J.L. Figueiredo, *Appl. Catal. B* 88 (2009) 550–556.
- [21] S.C. Kim, W.G. Shim, *Appl. Catal. B* 98 (2010) 180–185.
- [22] S.S.T. Bastos, J.J.M. Órfão, M.M.A. Freitas, M.F.R. Pereira, J.L. Figueiredo, *Appl. Catal. B* 93 (2009) 30–37.
- [23] M. Baldi, E. Finocchio, G. Busca, *Appl. Catal. B: Environ.* 16 (1998) 43–51.
- [24] M. Baldi, V.S. Escribano, J.M.G. Amores, F. Milella, G. Busca, *Appl. Catal. B* 17 (1998) 175–182.
- [25] C. Lahousse, A. Bernier, P. Grange, B. Delmon, P. Papaefthimiou, T. Ioannides, X.V. Kios, *J. Catal.* 178 (1998) 214–225.
- [26] B. Puértolas, A. Smith, I. Vázquez, A. Dejoz, A. Moragues, T. Garcia, B. Solsona, *Chem. Eng. J.* 229 (2013) 547–558.
- [27] K. Ramesh, L. Chen, F. Chen, Y. Liu, Z. Wang, Y.F. Han, *Catal. Today* 131 (2008) 477–482.
- [28] P. Mars, D. van Krevelen, *Chem. Eng. Sci., Spec. Suppl.* 3 (1954) 41–59.
- [29] J.C. Védrine, G. Coudurier, J.M. Millet, *Catal. Today* 33 (1997) 3–13.
- [30] J.C. Védrine, *Top. Catal.* 21 (2002) 97–106.
- [31] J.C. Védrine, J.M.M. Millet, J.-C. Volta, *Catal. Today* 32 (1996) 115–123.
- [32] J. Haber, M. Witko, *J. Catal.* 216 (2003) 416–424.
- [33] R.K. Grasselli, *Top. Catal.* 21 (1–3) (2002) 79–88.
- [34] K.D.M. Harris, P.P. Edwards, *Turning Points in Solid-State Materials and Surface Science*, RCS Publishing, Cambridge, 2008, pp. 568–576.
- [35] H.J. Shin, J.C. Kim, S.J. Lee, Y.P. Kim, *Environ. Sci. Pollut. Res.* 20 (2013) 1468–1481.
- [36] R.G. Derwent, M.E. Jenkin, M.J. Pilling, W.P.L. Carter, A. Kaduwela, *J. Air Waste Manag. Assoc.* 60 (2010) 914–924.
- [37] P. Yu, X. Zhang, Y. Chen, Y. Ma, *Mater. Lett.* 64 (2010) 61–64.
- [38] F. Kapteijn, L. Singoredjo, A. Andreini, J.A. Moulijn, *Appl. Catal. B* 3 (1994) 173–189.
- [39] E.R. Stobbe, B.A. de Boer, J.W. Geus, *Catal. Today* 47 (1999) 161–167.
- [40] W. Gac, *Appl. Catal. B* 75 (2007) 107–117.
- [41] F. Wang, H. Dai, J. Deng, G. Bai, K. Ji, Y. Liu, *Environ. Sci. Technol.* 46 (2012) 4034–4041.
- [42] Q.-F. Deng, T.-Z. Ren, Z.-Y. Yuan, *Reac. Kinet. Mech. Catal.* 108 (2013) 507–518.
- [43] Y. Yongnian, H. Ruili, C. Lin, Z. Jiayu, *Appl. Catal. A* 101 (1993) 233–252.
- [44] M. Kang, E.D. Park, J.M. Kim, J.E. Yie, *Appl. Catal. A* 327 (2007) 261–269.
- [45] R. Larachi, J. Pierre, A. Adnot, A. Bernis, *Appl. Surf. Sci.* 195 (2002) 236–250.
- [46] M. Zawadzki, J. Trawczynski, *Catal. Today* 176 (2011) 449–452.
- [47] Y. Liu, H. Dai, J. Deng, S. Xie, H. Yang, W. Tan, W. Han, Y. Jiang, G. Guo, *J. Catal.* 309 (2014) 408–418.
- [48] S. Ardizzone, C.L. Bianchi, D. Tirelli, *Colloids Surf. A: Physicochem. Eng. Asp.* 134 (1998) 305–312.
- [49] H.W. Nesbitt, D. Banerjee, *Am. Mineral.* 83 (1998) 305–315.
- [50] R.J. Iwanowski, M.H. Heinonen, W. Paszkowicz, R. Minikae, T. Story, B. Witkowska, *Appl. Surf. Sci.* 252 (2006) 3632–3634.
- [51] A.A. Davydov, *Infrared Spectroscopy of Adsorbed Species on the Surface of Transition Metal Oxides*, Wiley, Chichester, UK, 1990.
- [52] E. Finocchio, G. Busca, *Catal. Today* 70 (2001) 213–225.
- [53] V. Bolis, S. Bordiga, C. Lamberti, A. Zecchina, A. Carati, F. Rivetti, G. Spanò, G. Petrini, *Langmuir* 15 (1999) 5753–5764.
- [54] J.A. Lercher, C. Gründling, G. Eder-Mirth, *Catal. Today* 27 (1996) 353–376.
- [55] B. Bonelli, M. Cazzolino, R. Tesser, M. Di Serio, M. Piumetti, E. Garrone, E. Santacesaria, *J. Catal.* 246 (2007) 293–300.
- [56] L. Xu, X.-S. Li, M. Crocker, Z.-S. Zhang, A.-M. Zhu, *J. Mol. Chem. A: Chem.* 378 (2013) 82–90.
- [57] Z. Wu, B. Jiang, Y. Liu, H. Wang, R. Jin, *Environ. Sci. Technol.* 41 (2007) 5812–5817.
- [58] D. Barbera, F. Cavani, T. D'Alessandro, G. Fornasari, S. Guidetti, A. Aloise, G. Giordano, M. Piumetti, B. Bonelli, C. Zanzottera, *J. Catal.* 275 (2010) 158–169.
- [59] A. Zecchina, S. Bordiga, G. Spoto, L. Marchese, G. Petrid, G. Leofanti, M. Padovan, *J. Phys. Chem.* 96 (1992) 4991–4997.
- [60] F. Volkenstein, *The Electronic Theory of Catalysis on Semiconductors*, Pergamon Press, New York, 1963.
- [61] R.A. van Santen, M. Neurock, *Molecular Heterogeneous Catalysis*, Wiley-VCH, Verlag, 2006.
- [62] Z.-Y. Fei, B. Sun, L. Zhao, W.-J. Ji, C.-T. Au, *Chem. Eur. J.* 19 (2013) 6480–6487.
- [63] M. Hussain, N. Russo, G. Saracco, *Chem. Eng. J.* 166 (2011) 138–149.
- [64] M. Ruitenbeek, A.J. van Dillen, F.M.F. de Groot, I.E. Wachs, J.W. Geus, D.C. Koningsberger, *Top. Catal.* 10 (2000) 241–254.
- [65] G.I. Golodets, New developments in selective oxidation, in: G. Centi, F. Trifiro (Eds.), *Studies in Surface Science and Catalysis*, vol. 55, Elsevier, Amsterdam, 1990, p. 693.
- [66] G.K. Boreskow, Catalytic activation of dioxygen, in: J. Anderson, M. Boudart (Eds.), *Catalysis Science and Technology*, 3, Springer-Verlag, Heidelberg, 1982 (Ch. 3).